Available online at www.sciencedirect.com
ScienceDirect
Geochimica et Cosmochimica Acta 72 (2008) 4929–4947
Geochimica et Cosmochimica Acta
www.elsevier.com/locate/gca

Nitrogen geochemistry as a tracer of fluid flow in a hydrothermal vent complex in the Karoo Basin, South Africa

Henrik Svensen [a,*], Gray Bebout [b], Andreas Kronz [c], Long Li [b], Sverre Planke [a,d], Luc Chevallier [e], Bjørn Jamtveit [a]

[a] *Physics of Geological Processes (PGP), Department of Physics, University of Oslo, P.O. Box 1048, Blindern, Norway*
[b] *Department of Earth and Environmental Sciences, Lehigh University, Bethlehem, PA 18015-3188, USA*
[c] *Geowissenschaftliches Zentrum, University of Goettingen, Goldschmidt-Strasse 1, D-37077 Goettingen, Germany*
[d] *Volcanic Basin Petroleum Research (VBPR), Oslo Research Park, Oslo, Norway*
[e] *Council for Geoscience, P.O. Box 572, Bellville 7535, Cape Town, South Africa*

Received 28 January 2008; accepted in revised form 31 July 2008; available online 7 August 2008

Abstract

We have investigated the N geochemistry of minerals and rocks from contact metamorphic aureoles and hydrothermal vent complexes (HVC) in the Karoo Basin in South Africa. The HVC formed during phreatic eruptions associated with rapid devolatilization and pressure build-up in contact aureoles around early Jurassic sill intrusions. By combining outcrop data from a HVC and core data from contact aureoles, we investigate the relationship between light element release during metamorphism and vertical fluid migration. Sandstone and breccia from the HVC contain early-diagenetic ammonium NH_4^+-bearing feldspar (buddingtonite) and illite. Ammonium occupies up to 95% of the A site in feldspar, corresponding to concentrations up to 5.2 wt% N. Bulk-rock N isotope data for rocks from inside and outside the hydrothermal vent complex fall into two distinct groups. Background samples have $\delta^{15}N_{air}$ between +1.5‰ and +4.9‰, whereas minerals from the vent complex have $\delta^{15}N$ in the range +7.5 to +10.6‰. The N geochemistry of contact metamorphic shale from the lower stratigraphic units of the Karoo Basin shows that the vitrinite reflectance and $\delta^{15}N$ values are positively correlated. Shale with reflectivity values >4%Ro are enriched in ^{15}N, with $\delta^{15}N$ values between +6‰ and +14‰, implying the release of isotopically light N into metamorphic fluids (probably as N_2). We suggest that the relatively high $\delta^{15}N$ values of the early-diagenetic buddingtonite in the HVC reflect exchange of buddingtonite with N-bearing fluids ascending from greater depth after their release during contact metamorphism and dehydration. We present a qualitative model whereby hydrothermal vent complexes represent fluid flow structures after their formation, focusing N-bearing metamorphic fluids sourced in deeper levels of the basin. The release of organic N from sediments at depth in volcanic basins could play a role in the geochemical cycle of N, becoming particularly important during periods of intense volcanic activity.

---

1. INTRODUCTION

Upward migration of fluids in sedimentary basins commonly occurs through faults or through the formation of piercement structures associated with escape of overpressured fluids. Piercement structures include blow-out pipes, mud volcano conduits, and hydrothermal vent complexes (e.g., Jakubov et al., 1971; Brown, 1990; Planke et al., 2003, 2005; Svensen et al., 2004, 2007; Berndt, 2005). Such structures may represent important secondary migration pathways for basinal fluids including petroleum. The geochemistry of minerals from these pipes and corresponding seep deposits may help to identify the source and composition of paleo-fluids. In particular, the stable isotopes of carbon in carbonates from seep deposits are widely used as tracers (Hovland et al., 1987; Paull et al., 1992; Svensen

---

[*] Corresponding author.
E-mail address: hensven@fys.uio.no (H. Svensen).

0016-7037/$ - see front matter © 2008 Elsevier Ltd. All rights reserved.
doi:10.1016/j.gca.2008.07.023

et al., 2003; Mazzini et al., 2005). In this paper, we focus on N isotopes as tracers of fluid flow in piercement structures formed by devolatilization reactions and boiling in contact aureoles around mafic sill intrusions in the Karoo Basins.

During shallow diagenesis in sedimentary basins, organic matter, petroleum and clay minerals are the three the main N reservoirs capable of releasing nitrogen. The oxidation and bacterial breakdown of organic material induces gas production and controls N isotope fractionation. In general, light nitrogen (N with relatively low $^{15}N/^{14}N$) is preferentially released and may subsequently be incorporated into the mineral lattices of authigenic NH_4^+-rich feldspar (buddingtonite) and clay minerals (e.g., illite), both of which act as N sinks in many basin settings (e.g., Loughnan et al., 1983; Williams et al., 1989, 1992, 1995; Ramseyer et al., 1993). The isotopic fractionation associated with the degassing process causes N remaining in the source rock to become enriched in ^{15}N. No significant fractionation occurs between the N isotopes in pore fluids and in coexisting clay minerals at diagenetic conditions (Williams et al., 1995). During low-grade metamorphism ($T < 300$ °C), the ambient oxygen fugacity determines whether molecular nitrogen gas (N_2) or ammonia (NH_3) is produced from breakdown of organic material (e.g., Froelich et al., 1979; Krooss et al., 1995). The released N is incorporated into, and retained at remarkably high concentrations, in mineral lattices particularly in the micas throughout the metamorphic cycle to temperatures beyond those of partial melting (e.g., Haendel et al., 1986; Bebout and Fogel, 1992; Bebout et al., 1999; Sadofsky and Bebout, 2000). The variation in isotopic composition among N reservoirs implies that the N isotopic composition of minerals can serve as tracers of fluid sources (e.g., Williams et al., 1995; Bebout, 1997; Zhu et al., 2000; Jia et al., 2003; Jia and Kerrich, 2004; Elkins et al., 2006).

In this paper, we report on the diagenetic evolution of sedimentary rocks and breccia deposits from one hydrothermal vent complex in the volcanic Karoo Basin, South Africa. The main emphasis is buddingtonite petrography and geochemistry. The geological setting and formation mechanisms of the HVC have been treated separately (Jamtveit et al., 2004; Svensen et al., 2006), as well as the implications for the early Jurassic climate (Svensen et al., 2007). Our primary goals in this paper are to (1) characterize the authigenic petrography of a hydrothermal vent complex in the Karoo Basin, (2) compare the N geochemistry of metamorphosed organic-rich shale in the Karoo Basin with the N geochemistry of minerals from the vent complex, (3) evaluate the various sources of N (i.e., minerals, organic material, coal, dolerite intrusions) contributing to mineral-bound N in a pierced-basin setting, and (4) test whether the hydrothermal vent complexes are short lived or long term fluid flow structures in the Karoo Basin.

2. GEOLOGICAL BACKGROUND AND MATERIALS

2.1. The Karoo Basin

The Karoo Basin (Fig. 1) covers more than half of South Africa. The basin is bounded by the Cape Fold Belt along its southern margins and comprises up to 6 km of clastic sedimentary strata capped by at least 1.4 km of basaltic lava (e.g., Smith, 1990; Johnson et al., 1997). The sediments were deposited from the Late Carboniferous to the Middle Jurassic, in an environment ranging from partly marine (the Dwyka and Ecca groups) to fluvial (the Beaufort Group and parts of the Stormberg Group) and aeolian (upper part of the Stormberg Group) (Veevers et al., 1994; Catuneanu et al., 1998). Organic-rich shale (the Whitehill Formation) dominates the Ecca Group, with total organic C contents locally reaching 15 wt% (Faure and Cole, 1999). The Ecca Group reaches hundreds of meters in thickness in the western parts of the basin, and is commonly intruded by sill intrusions. The Whitehill Formation, which pinches out towards the east and is replaced by the time-equivalent Vryheit Formation (e.g., Veevers et al., 1994). The Stormberg Group includes the Molteno Formation (coarse sandstone, shale, and coal), the Elliot Formation (sandstone, shale; “red beds”), and the Clarens Formation (sandstone with occasional siltstone horizons).

Both southern Africa and Antarctica experienced extensive volcanic activity in early Jurassic times, at about 183 Ma. Dolerites and lavas of the Karoo-Ferrar Large Igneous Province were emplaced and erupted within a relatively short time span (183 ± 1 Ma;), and the main phase lasted less than 1 m.y. (Duncan et al., 1997; Jourdan et al., 2005). Sills and dikes are present throughout the sedimentary succession in the Karoo Basin (Fig. 1) (Chevallier and Woodford, 1999; Polteau et al., 2008), where they locally comprise up to 70% of the stratigraphic thickness (Rowsell and De Swardt, 1976).

An important by-product of intrusive activity in sedimentary basins is rapid heating of the intruded sediments and their pore fluids, locally leading to pore fluid expansion and boiling, and to metamorphic reactions. These processes may also lead to the formation of hydrothermal vent complexes in the upper 1 km in the basin, mostly cropping out in the Stormberg Group (e.g., Jamtveit et al., 2004). In the case of the Karoo Basin, the HVC represent pipe-like piercement structures formed in a subaerial basin setting (Svensen et al., 2006). More than 500 hydrothermal vent complexes are mapped in the Karoo Basin, and the complexes range from almost purely volcanic to almost entirely filled with sedimentary material (e.g., Dingle et al., 1983; Jamtveit et al., 2004; Svensen et al., 2006). In addition, thousands of breccia pipes are located in the Western Karoo Basin, where they formed in contact aureoles in black shale. We have recently proposed that the contact metamorphism and breccia pipes released carbon gases to the atmosphere and triggered the Toarcian global warming (Svensen et al., 2007).

In this study, the N geochemistry was mainly studied on samples from the Witkop III hydrothermal vent complex (Fig. 1), where authigenic buddingtonite is common. Two samples from other vent complexes are included as reference material. In addition, we have studied the bulk N geochemistry of organic-rich shale from the Ecca Group collected from two boreholes with sill intrusions.

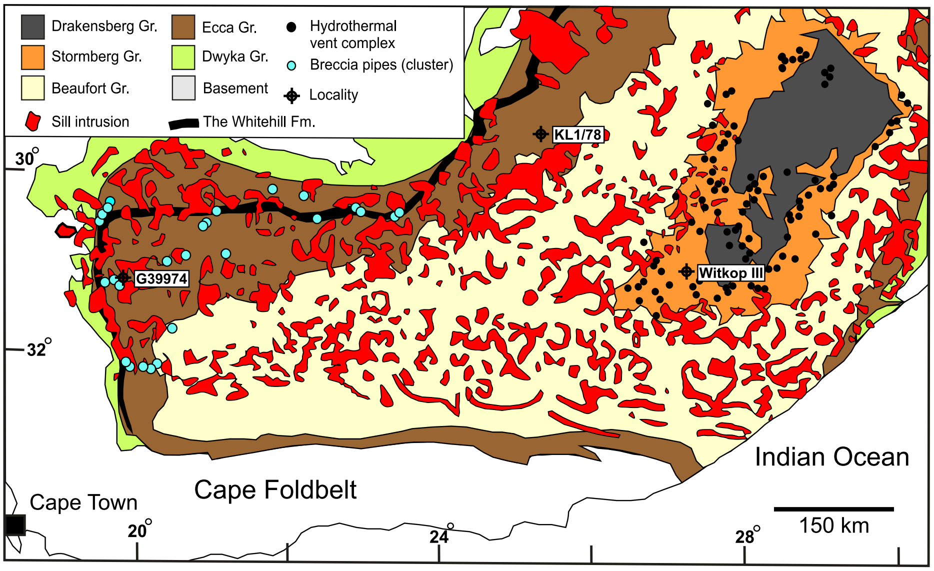

Fig. 1. Distribution of sills, hydrothermal vent complexes, and breccia pipes in the Karoo Basin, South Africa. The hydrothermal vent complexes are mainly confined to outcrops in the Stormberg Group sediments, whereas the breccia pipes are confined to the Ecca and Beaufort groups (Svensen et al., 2007). Data presented in this paper come from the Witkop III hydrothermal vent complex, with additional borehole data (labeled KL1/78 and G39974. The map is modified from (Svensen et al., 2007). Note that the symbols for the breccia pipes represent pipe clusters and not individual pipes. See Svensen et al. (2006) for a simplified basin stratigraphy and location of hydrothermal vent complexes.

2.2. Hydrothermal vent complex sampling localities

The studied samples are mainly from one sediment-dominated hydrothermal vent complex in the Eastern Cape; the Witkop III locality. All samples are from surface exposures, except a few from a borehole that was drilled at the edge of the complex, penetrating mostly zeolite-cemented sandstones and background sediments (Svensen et al., 2006). Two reference samples were added to the data set, one from a vent complex close to Witkop III (called Witkop II), and the other from a vent complex close to Jamestown (Table 1). Generally, all localities contain sediment breccias piercing the Stormberg Group sediments (Svensen et al., 2006).

The Witkop III complex is geologically divided into an inner and outer zone (Fig. 2). The outer zone comprises structurally modified Clarens Formation strata with dips ranging from background values (~5°) to about 60° toward the inner zone of the complex. The total width of the complex is about 700 m, 400 m of which is taken up by the inner zone. The inner zone of the Witkop III complex is characterized by tilted blocks of Clarens Formation sandstone intruded and overlain by sediment breccia (see Svensen et al., 2006 for details). Geological mapping of Witkop III revealed the presence of distinct facies units including sandstone (Unit I), zeolite-cemented sandstone (Unit II), and sediment breccia (Unit III). Zeolite cement in sandstone is interpreted to have precipitated from hydrothermal solutions shortly after the formation of the complex, and typically is the only hydrothermal mineral identified (Svensen et al., 2006). The breccia contains fragments of sandstone, siltstone, and shale. The clasts in the breccia are sourced from both the Clarens Formation and deeper formations. Organic-rich rocks or clasts are absent from the Witkop III complex, where the content of igneous material is negligible.

The sediment-dominated hydrothermal vent complex near Jamestown has not been mapped or sampled in detail, but the sample included here (B-11) is representative of the bulk of the sediment fill.

2.3. Contact aureoles

For comparison with the HVC samples, we have also sampled both unmetamorphosed and contact metamorphosed shale samples from the KL1/78 and G39974 boreholes (Fig. 1). The first is a well-known reference borehole for the Ecca Group in the northern parts of the basin (Faure and Cole, 1999). The organic-rich shale in this borehole is intruded by a 15-m-thick mafic sill intrusion, with a pronounced contact aureole. The second borehole is located in the Ecca Group of the western Karoo Basin. Here, the organic-rich shale is intruded by several thick (~100 m) sill intrusions, and the borehole is located close to several breccia pipes formed due to overpressure generated by the devolatilization reactions (Svensen et al., 2007). The boreholes are located far from the Witkop III HVC, but the boreholes are nevertheless relevant because equivalent Ecca Group sediments are present throughout the basin. The Ecca Group is located at about 2400 m depth underneath the Witkop III complex, based on borehole data 50 km from Witkop III (borehole WE1/66; Leith and Trümpelmann, 1967). Furthermore, we attempt to use these boreholes as reference cases for the release of N from shale during contact metamorphism.

Table 1
Overview of samples and rock types from hydrothermal vent complexes

Sample	Locality	GPS coordinates		Setting
		(South)	(East)	
Sandstone (Unit I)				
K01HS-56	Witkop III	31 12′ 11.3″	27 13′ 44.4″	Sandstone
K02HS-29	Witkop III	31 12′ 10.8″	27 13′ 44.4″	Conglomerate
HS-35	Witkop III	31 12′ 09.2″	27 13′ 47.7″	Borehole, Clarens F.
HS-19I	Witkop III	31 12′ 09.2″	27 13′ 47.7″	Borehole, Elliot Fm.
HS-216	Witkop III	31 12′09.2″	27 13′ 47.7″	Borehole, Elliot Fm.
HS-259	Witkop III	31 12′ 09.2″	27 13′ 47.7″	Borehole, Elliot Fm.
K02HS-22	Witkop III	31 12′ 10.9″	27 13′ 45.8″	Border of ss pipe
K03HS-22	Witkop II	31 15′ 31.3″	27 09′ 49.2″	Ss cutting breccia
Zeolite sandstone (Unit II)				
K01HS-44	Witkop III	31 11′ 55.9″	27 13′ 49.1″	Zeolite-cemented Clarens
K01HS-49	Witkop III	31 11′ 57.4″	27 13′ 52.1″	Zeolite-cemented Clarens
K01HS-47	Witkop III	31 11′ 58.3″	27 13′ 49.0″	Clarens Fm. /outer zone
Sediment breccia (Unit III)				
K02HS-15	Witkop III	31 12′ 05.7″	27 13′ 46.8″	Cc-cemented sandstone
K02HS-16	Witkop III	31 12′ 06.5″	27 13′ 46.6″	Breccia, ss matrix
K02HS-19	Witkop III	31 12′ 15.3″	27 13′ 38.2″	Breccia dyke
K02HS-26	Witkop III	31 12′ 10.5″	27 13′ 45.4″	Breccia pipe
K02HS-2K	Witkop III	31 12′ 11.6″	27 13′ 44.9″	Breccia pipe
B-11	Jamestown	31 12′ 08.8″	26 13′ 40.2″	Breccia, ss matrix

3. METHODS AND ANALYTICAL TECHNIQUES

3.1. Petrography

The petrography of authigenic minerals has been studied by optical and electron microscopy,in part using the JEOL JSM 840 scanning electron microscope (SEM) located at the Department of Geosciences, University of Oslo. The presence of a buddingtonite component in authigenic K-feldspar was indicated by anomalously low K signals during SEM EDX analyses, and by zoning in the feldspar. The presence of N in the feldspar was later confirmed by electron microprobe analyses (see below).

3.2. Analyses of organic matter

Bulk-rock powders were analyzed for total organic carbon (TOC) and vitrinite reflectance at Applied Petroleum Technology, Kjeller, Norway. Acid treatment of the powders was done to quantify the content of inorganic C (presumed to be present as carbonate; <0.2 wt% in all samples). The TOC was estimated using a Rock-Eval 6 instrument during oxidation to CO/CO_2 in the temperature range 300–650 °C. For vitrinite reflectance measurements, powders were treated with hydrochloric and hydrofluoric acid before kerogen embedment in epoxy. Polished slabs were analyzed on a Zeiss MPM 03 photometer microscope equipped with an oil objective. The reflectance measurements were calibrated against several standards. At least 20 measurements were made per sample, and the results are reported as percent reflectivity in oil (%Ro). The quality of the analyses depends on the abundance and type of vitrinite, particle size and surface quality, and the uncertainty is typically below 10%.

3.3. Electron microprobe analyses

Wavelength dispersive electron microprobe analyses of the K-feldspar–buddingtonite series were performed using a JEOL JXA 8900 RL instrument at the Geowissenschaftliche Zentrum Goettingen, equipped with 5 WDS detectors. For quantitative measurements, 15 kV acceleration voltage, 12 nA beam current and counting times between 10 s (Na), 15 s (K, Ca, Al, and Si), 20 s (N and O), and 30 s (Ba) on the peak of each specific Kα-line were chosen. Due to the general difficulties of analyzing light elements in minerals from thin sections, we elaborate on the details of our N electron microprobe analytical technique. NH_4-feldspar decomposes very rapidly under the electron beam (Kronz and Pöter, 1999). Beam diameters between 8 and 20 μm were used to minimize this effect. This decomposition behavior does not allow for the usage of higher beam currents or increased counting times, which limits the detection efficiency of the light elements N and O. From the given beam and counting conditions we get an absolute precision (2σ, and values in wt%) of O: 0.6, N: 0.2, Na: 0.06–0.1, K: 0.1–0.2, Ca: 0.02, Al: 0.1, Si: 0.2, Fe: 0.04, and Ba: 0.1–0.15.

EMP analysis of light elements is hampered by their large mass-absorption coefficients (MAC). Absorbance of O–Kα X-rays by N (MAC: 17,300 $cm^2\ g^{-1}$, (Bastin and Heijligers, 1988) leads to large correction factors for the fluorescence and absorption corrections of N–Kα and O–Kα raw counts, respectively. For this reason O is

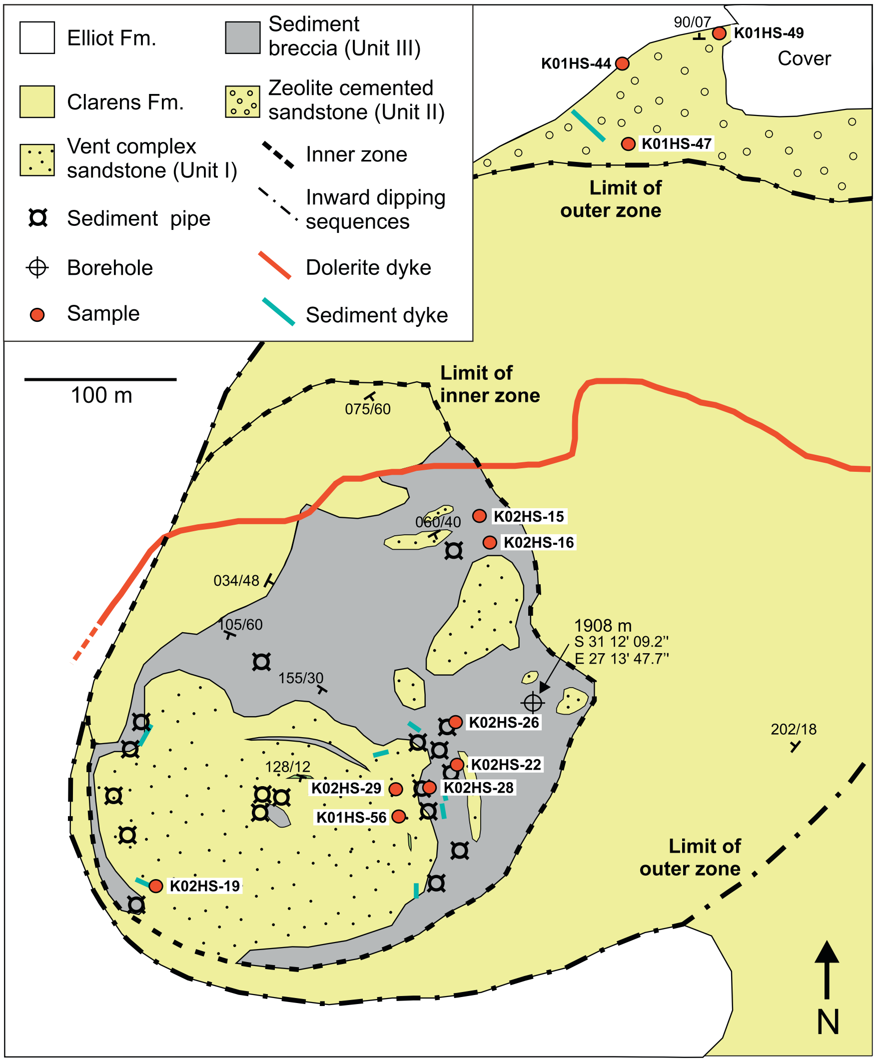

Fig. 2. The geology of the Witkop III hydrothermal vent complex. The complex is divided into an inner and an outer zone, where the outer zone represents dipping Clarens Formation sandstone (locally with zeolite cement), and the inner zone comprise sediment breccia overlain by sandstone. The map is modified from Svensen et al. (2006), and is based on an aerial photo projection. Samples used in this study are shown on the map, with GPS coordinates given in Table 1.

analyzed precisely, and not estimated from the usual stoichiometric calculations. The following standards were used for calibration: synthetic buddingtonite for N (Pöter et al., 1999), gem quality orthoclase for O (Arnaud and Kelley, 1997), albite for Na, Al_2O_3 (synthetic) for Al, wollastonite for Si and Ca, sanidine for K, hematite for Fe, and celsiane for Ba. Matrix correction was performed applying the ϕ–ρ–z method by Armstrong (1995).

Due to the general small fluorescence yield of emitted characteristic X-rays from light elements a high-performance analyzing-crystal, LDEN (2*d* spacing of 80 Å, ScCr-multilayer pseudocrystal), was chosen for the acquisition of the N–Kα signal. The development of "Layered Dispersion Element" crystals (LDE) enables the quantification of ultra-light elements at low amounts by EMP (Armstrong, 1988; Rybka and Wolf, 1995). Due to its build-up of Cr/Sc multilayers (both elements of low MAC on N–Kα), the intensity yield of the LDEN crystal is ten times higher compared to the usual LDE1 ($2d = 60$ Å, W/Si multilayer).

Carbon coating was applied simultaneously on the N/O standards and the samples to equalize the large absorption effects by the coating material (absorbance of N–Ka in C: MAC 25,500 $cm^2\ g^{-1}$). To avoid contamination-effects by a C build-up at the surface on the measurement spot (Raudsepp, 1995), a liquid N trap was used to freeze carbon hydrates off from the vacuum chamber.

Element distribution of N, Na, K, Ca, and Ba (WDS) was mapped using an acceleration voltage of 15 kV and a beam current of 15 nA. Acquisition times were chosen between 40 and 50 ms per step. The scan grid was spaced at 0.5-µm steps, using 400–550 steps depending upon the dimension of each crystal. Simultaneous acquisition of the backscatter signal in composition mode was performed.

3.4. XRD

X-ray diffraction analyses were performed on clay fractions of crushed bulk-rock samples. The clay mineral fraction (<2 μm) was separated by settling in columns with deionised water. The clay fraction was then filtered through 0.45 μm pore size filter and saturated with $MgCl_2$, and mounted on silica plates before analyzed on a Philips X'Pert MPD at the Department of Geosciences, University of Oslo. Multiple runs followed standard procedures on untreated clay, after overnight treatment with ethylene glycol in an excicator at 60 °C, and after heating at 550 °C for 2 h.

3.5. Stable isotopes of nitrogen

Bulk-sediment samples were gently crushed by hand in a mortar followed by separation of the crushed material into silt- and sand-sized fractions. This allowed a crude separation of the clay minerals and the buddingtonite-bearing fraction. These splits, and also some bulk-sediment samples and kerogen separates, were sealed in quartz tubes with a $Cu–Cu_xO_x$ mixture after overnight evacuation. The tubes were then combusted at 1050 °C for 3 h (see Bebout and Fogel, 1992; Sadofsky and Bebout, 2000). Nitrogen concentration was determined by measuring the *m/z*-28 signal for calibrated inlet volumes in the mass spectrometer. Nitrogen isotope analyses were obtained using a Finnigan MAT 252 mass spectrometer in dual-inlet mode. The $\delta^{15}N$ values are reported relative to atmospheric N_2 $(^{15}N/^{14}N)_{std}$:

$$\delta^{15}N_{air} = \left[\frac{(^{15}N/^{14}N)_{sample} - (^{15}N/^{14}N)_{air}}{(^{15}N/^{14}N)_{air}}\right] \times 10^3$$

The reproducibility of the measured $\delta^{15}N$ (1σ for $\geqslant 3$ replicate analyses) was better than 0.2‰ and uncertainties for duplicate N concentration measurements were less than 5%.

4. DIAGENESIS AND GEOCHEMISTRY OF THE HYDROTHERMAL VENT COMPLEX

4.1. Diagenesis

The porosity of the samples collected at the surface is very high (up to 25%) due to weathering (Figs. 3 and 4). As a consequence, the matrix clay minerals are often absent, hampering a full investigation of their diagenetic evolution. However, clay fraction XRD analyses show that illite is the dominant clay mineral in most samples from all Units, with trace amounts of chlorite (Table 3). This is consistent with results from the Witkop I hydrothermal vent complex west of the study area (Sali Lorentzen, 2004) where well-preserved authigenic illite is present in

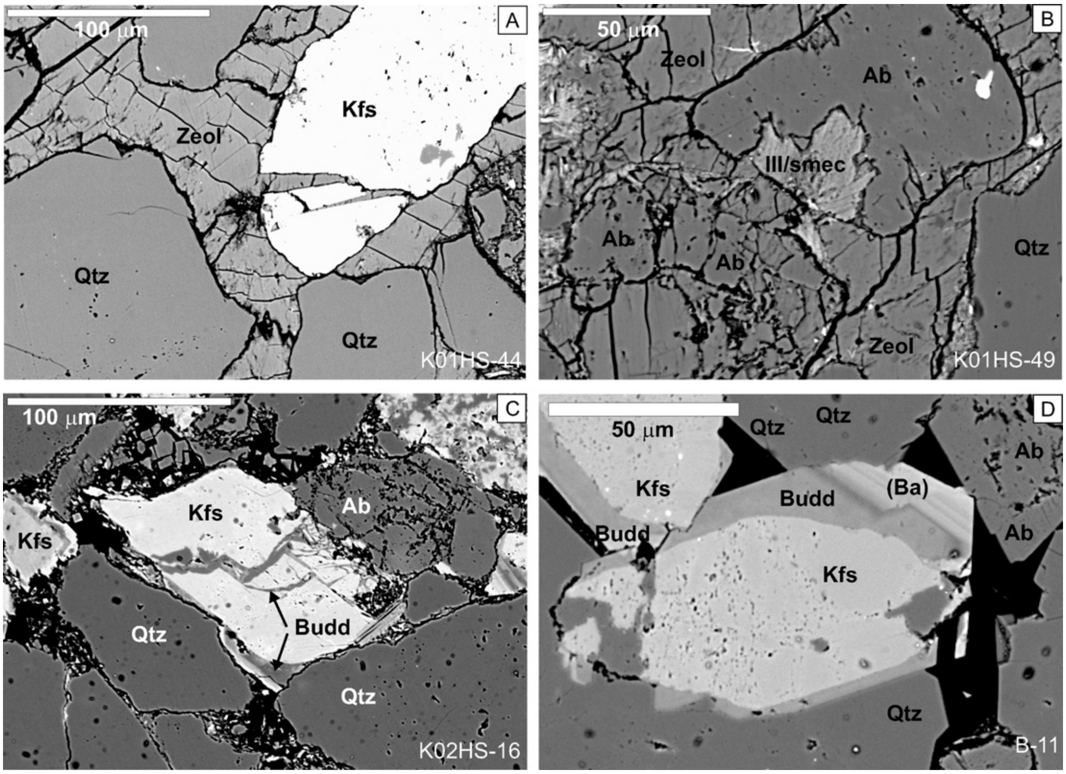

Fig. 3. Petrography of authigenic minerals from sandstone at Witkop III. (A) Zeolite-cemented sandstone facies. The SEM backscatter image shows early stage zeolite (laumontite) cement. Note the absence of authigenic quartz. (B) SEM backscatter image from a zeolite-cemented sandstone showing partially dissolved albite filled with illite/smectite and zeolite. Note that the illite/smectite texturally apparently predates the zeolite. (C) SEM backscatter image of sandstone from the breccia showing buddingtonite as fracture fill in K-feldspar and as overgrowths. The high porosity (black) is due to weathering. (D) SEM backscatter image of a sandstone from sandstone showing authigenic buddingtonite overgrowths on K-feldspar. Authigenic albite covers an albite grain whereas authigenic quartz apparently postdates buddingtonite.

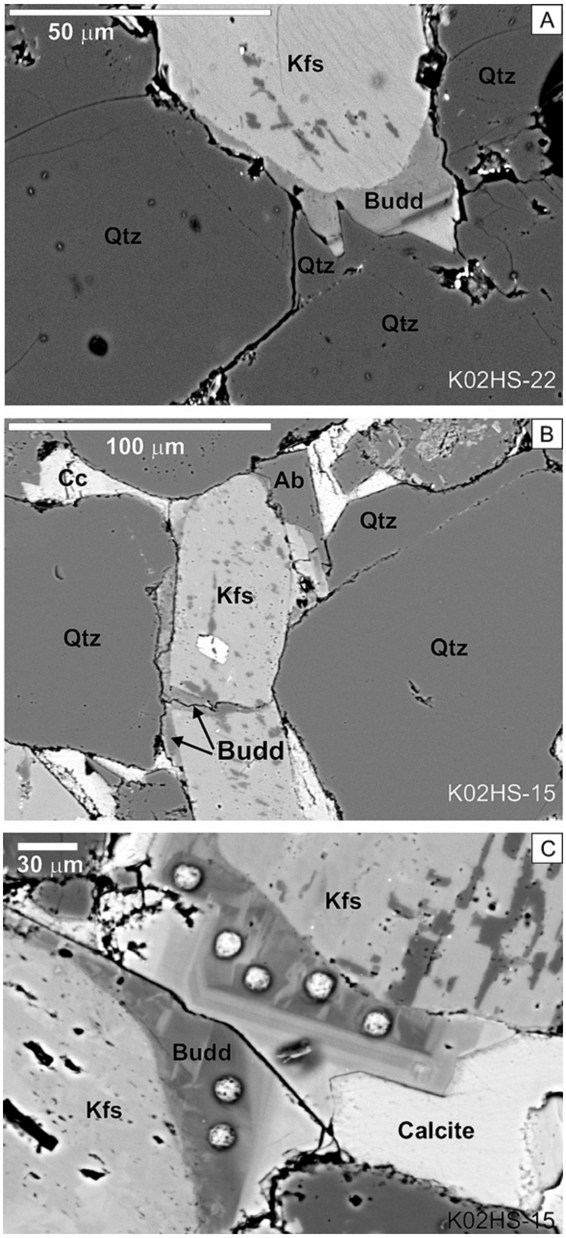

Fig. 4. SEM backscatter images of authigenic minerals from sediment breccias at Witkop III. (A) Zoned buddingtonite forms overgrowths on detrital K-feldspar. The autigenic feldspar is zoned, where barium-enriched feldspar texturally postdates the buddingtonite. (B) Sandstone matrix from a sediment breccia, showing a fractured feldspar grain with buddingtonite fracture fill. (C) Sandstone clast from sediment breccia. The authigenic buddingtonite reveals a complex zoning. The gray spots in the buddingtonite represent burns from the electron microprobe beam. Calcite is the pore filling mineral.

sandstone. The textural relationships of the chlorite remain uncertain due to the poor preservation of relevant textures. A schematic summary of the interpretation of the hydrothermal vent complex diagenesis is presented in Fig. 5 and is further described below. The background diagenetic evolution of the Clarens Formation in the Witkop III region, i.e., outside the hydrothermal vent complex, is similar to that of the vent complex except that the background sediments lack buddingtonite and zeolite.

4.1.1. Unit II (zeolite sandstone)

Laumontite is the dominant authigenic mineral in zeolite sandstone (Unit II) from the outer zone of the Witkop III hydrothermal vent complex (Svensen et al., 2006), where it is based on textures the earliest mineral that precipitated. Here, laumontite fills fractures in grains and forms pore-filling cement in sandstone where no authigenic quartz or feldspar is present (Fig. 3A and B). Laumontite is locally replacing albite (Fig. 3B), whereas some of the albite dissolution porosity has acted as precipitation sites for clay minerals (illite/smectite). Buddingtonite has not been found in the zeolite sandstone unit, possibly due to the coating effect of the zeolite (preventing formation of overgrowths), as suggested by the textures from Fig. 3A.

4.1.2. Units I and III

Relevant textures from inner-zone sandstone without zeolite cement (Unit I and the matrix of Unit III) suggest

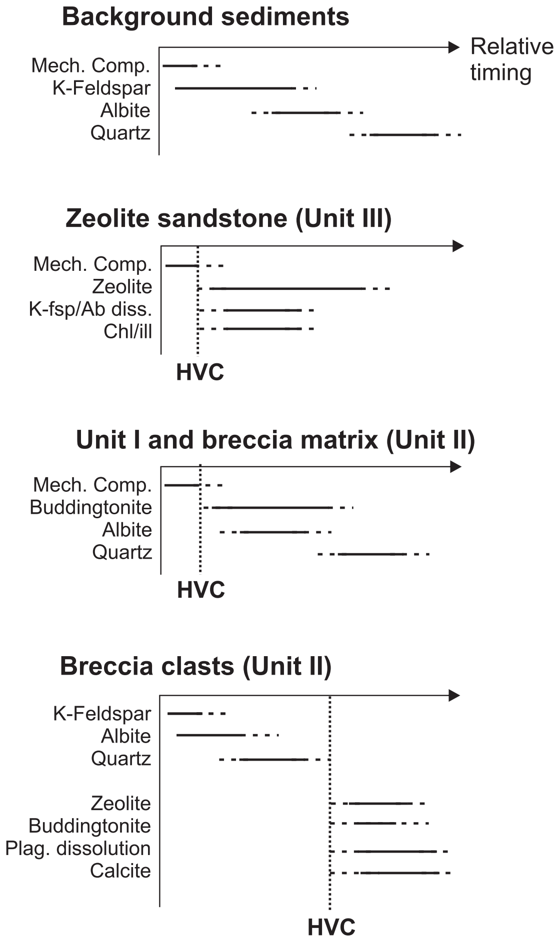

Fig. 5. Schematic diagenetic sequence based on SEM petrography from Witkop III. The diagram is divided into samples from outside the vent complex ("Background"), and from Units I and II. The timing of hydrothermal vent complex formation (and hence sill emplacement at depth) is shown as a vertical line labeled "HVC".

that authigenic albite and quartz postdate buddingtonite (Fig. 4A). Buddingtonite occurs as overgrowths and fracture-fill in detrital K feldspars (Fig. 3C). The buddingtonite overgrowths are usually strongly zoned, with well-developed intra-sector and sector zoning, and the zoning is due to variations in the buddingtonite and K/Ba-feldspar components (Fig. 6).

Within clasts from the sediment breccia, authigenic buddingtonite, albite, and quartz, occurs together with calcite (Fig. 4A and B). This authigenic mineralogy is present in large breccia boulders (as represented by sample K02HS-15). Although difficult to determine from the textural relations in the breccia clasts, we regard the albite and quartz as a part of the pre-vent complex mineralogy, whereas buddingtonite and calcite precipitated in the matrix after the clasts were incorporated into the breccia (Fig. 4C). We also regard it as most likely that any zeolite in the breccia clasts were formed after breccia formation. Calcite is found in several matrix samples from all units, but in all cases as sporadic remnants after surface erosion. We hypothesize that this calcite represents the same precipitation event as the breccia boulders.

4.2. Nitrogen geochemistry of the hydrothermal vent complex

4.2.1. Feldspar mineral chemistry

More than 100 point analyses of K-feldspar show significant differences in Na, N, and Ba concentration between detrital and authigenic K-feldspar (Fig. 7). Representative electron microprobe analyses (Table 2) document that the detrital feldspar lacks N, and has higher Na concentrations than that of the authigenic feldspar (Fig. 7). Barium is commonly present in the authigenic feldspar as a trace component, but reaches 1–1.5 wt% in several instances. Barium concentrations in detrital and authigenic feldspar do not correlate with N concentration, in contrast with the findings of others (e.g., Orberger et al., 2005). However, this is likely due to low Ba concentrations in the analyzed authigenic feldspar, as element mapping shows that high Ba is confined to zones with high N (Fig. 6).

Most of the authigenic feldspar has N concentration between 1 and 5 wt%. When recalculated to structural formulas, the buddingtonite component varies from near 0 to about 95 mole % (Table 2, Fig. 8). Nitrogen is present in the crystal lattice of K-feldspar as NH_4^+, and occupies the A site where it substitutes for K. The exchange can be written as:

$$KAlSi_3O_8 + NH_4^+ \leftrightarrow NH_4AlSi_3O_8 + K^+$$

The buddingtonite component of the authigenic feldspars ranges from 0.0 to 0.9 mole %. Only one analysis falls in the 0.35- to 0.5-mole % range (Fig. 8). There are no obvious compositional trends in the buddingtonite component versus rock type or Unit at Witkop III, neither is there any systematic difference between fracture fill and overgrowth composition. It should be noted that due to the complex buddingtonite zoning and the size of the electron beam (8–20 μm), some of the analyses likely represent mixtures of two or more feldspar compositions. SEM imaging and microprobe element mapping demonstrate the presence of sector and intra-sector zoning (Fig. 6). In many cases, the last stage of feldspar cement is dominated by K-feldspar, and buddingtonite is confined to early and intermediate stages. In Fig. 6, buddingtonite is overgrown with K-feldspar containing less that 1% N.

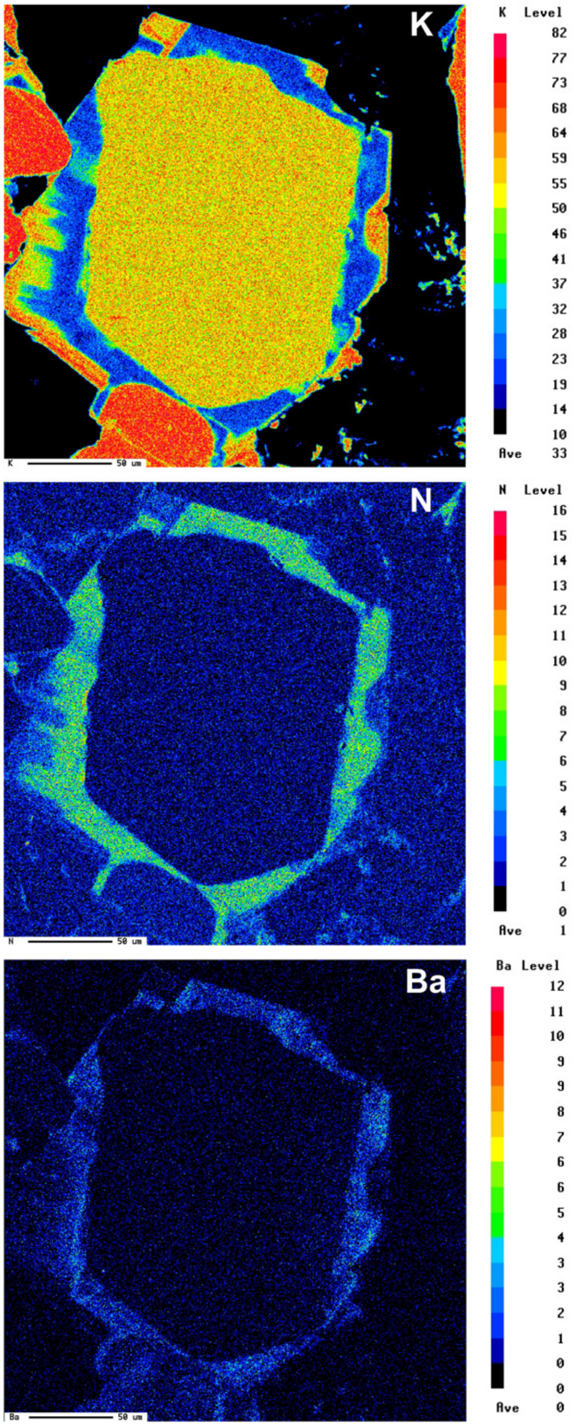

Fig. 6. Electron microprobe element mapping of potassium and N in a detrital K-feldspar grain with authigenic overgrowths. Note the homogeneous feldspar core, and the irregular zoning. The buddingtonite-rich inner zoning is overgrown by N-poor feldspar.

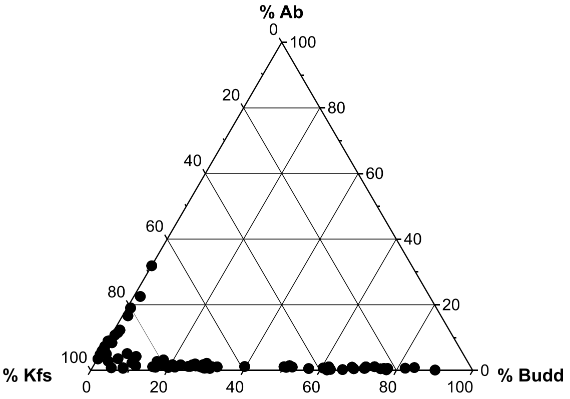

Fig. 7. Electron microprobe results showing the normalized composition of detrital and diagenetic K-feldspar. The detrital feldspars contain no or very little N, but are rich in Na. The authigenic feldspars contain up to 5 wt% N.

4.2.2. Nitrogen isotopes

The N isotope analyses of split silt and sand samples together show a range in $\delta^{15}N_{air}$ values from +1.5‰ to +10.6‰ (Table 3). The data for the sand fractions approximate the $\delta^{15}N$ values in buddingtonite (due to the large grain size of feldspar in the samples), whereas the silt fraction is thought to represent the $\delta^{15}N$ values of clays (mainly illite, due to the small grain size of the clays), likely with some contamination from finely crushed buddingtonite. The range in N concentration is similar for the samples from the silt and the sand fractions (530–2522 ppm). One sandstone sample (K01HS-47) has an elevated N concentration of 5959 ppm that can be explained by a high modal content of buddingtonite.

The results may be grouped according to geological setting (Fig. 9), where Group I represents samples from the outer zone (i.e., the Elliot and Clarens formations; $\delta^{15}N$ = +1.5‰ to +4.9‰), and Group II represents sandstone and breccia from inside the Witkop III complex ($\delta^{15}N$ = +7.5‰ to +10.6‰). Within both groups, buddingtonite and illite show the same range in $\delta^{15}N$, although the silt fraction samples consistently have somewhat higher $\delta^{15}N$ values than sand fraction samples. The Group I geochemistry reflects illite $\delta^{15}N$ values as buddingtonite is absent except for in the K01HS-47 sample. The samples with zeolite cement do not differ in $\delta^{15}N$ from the other Group I samples.

4.3. Nitrogen geochemistry of contact aureoles

The vitrinite reflectivity values of the Ecca Group shale from the two boreholes (KL1/78 and G39974) show a range in metamorphism from close to background values (%Ro = 1.34) to high-grade metamorphism (%Ro = 7.9; Table 4). Although not demonstrated here, the increase in vitrinite reflectivity in G39974 corresponds with the distance from the intrusive contact, and total organic C content also decreases across this traverse (Svensen et al., 2007). In this paper, we use the vitrinite reflectivity, and not the distance from the intrusive contact, as a proxy for metamorphic grade, enabling us to compare samples from different settings with different background TOC concentrations. The N concentrations are generally higher in the kerogen extracts, demonstrating that much of the N is bound to organic matter. Maximum N concentrations in kerogen extracts reach 4240 ppm and $\delta^{15}N$ values of these samples range from +3.8‰ to +14.2‰. There is a positive correlation between vitrinite reflectivity and $\delta^{15}N$, with the least metamorphosed samples having the lowest $\delta^{15}N$ (near +4‰; Fig. 10A). At reflectivity values above 4, the $\delta^{15}N$ values show a wide range, from +6‰ to +14.2‰. Three samples with reflectivity values above 7 have $\delta^{15}N$ values in the upper end of this range. A similar trend emerges when comparing the vitrinite reflectivity with the N/TOC ratio (Fig. 10B). Low-grade metamorphic samples (with %Ro $\leqslant$ 4) have the lowest N/TOC, with a significant increase above %Ro ~ 4. The N/TOC ratio reaches 9.5 in the highest-grade sample.

5. DISCUSSION

5.1. Timing of buddingtonite cement

The petrography of more than 20 samples from hydrothermal vent complexes suggests that buddingtonite and zeolite (laumontite) formed during early diagenesis. Both minerals occur as fracture fill in K-feldspar, suggesting that precipitation occurred when the sediments compacted mechanically (cf. Ramseyer et al., 1993). Mechanical compaction commonly dominates in the first 1000 m of burial (e.g., Worden and Burley, 2003). The laumontite is assumed to have precipitated from low temperature hydrothermal fluids shortly after the formation of the Witkop III hydrothermal vent complex (Svensen et al., 2006), mainly localized along permeable sandstone horizons. Thus the laumontite cement may have inhibited later quartz precipitation. Furthermore, the buddingtonite precipitation was pervasive throughout the inner zone of the vent complex, whereas it is absent in the outer zone. From the textural relationships between buddingtonite, laumontite, and quartz, we suggest that buddingtonite precipitated at fairly low temperatures, below the normal onset of quartz cementation (i.e., below 70–80 °C; e.g., Walderhaug, 1994; Giles et al., 2000). This is in agreement with buddingtonite data from other early-diagenetic sequences, where buddingtonite may have formed at temperatures below 30 °C (Ramseyer et al., 1993). The rapid decrease in the buddingtonite component during feldspar growth may be interpreted as a sudden reduction in the N concentration of the fluid phase, reflecting the large-scale fluid circulation of an essentially open system.

5.2. Timing of quartz cement

The onset of quartz cementation in the Stormberg Group sediments depended on the geothermal gradient and possible heat input from the hydrothermal vent complex during burial. On the basis of our data from the Clarens Formation and Witkop III and data for authigenic quartz from the Clarens, Elliot, and Molteno Formations

Table 2
Electron microprobe analyses of selected representative detrital and authigenic K-feldspar/buddingtonite

Sample	KO2HS-16	K02HS-16	KO1HS-47	KO1HS-47	KO1HS-47	KO1HS-47	K01HS-47	KO1HS-56	KO1HS-56	KO1MS-56	KO2HS-15	KO2HS-15	KO2HS-22
wt%	Detrital	Authigenic	Detrital	Authigenic	Authigenic	Authigenic	Authigenic	Detrital	Authigenic	Authigenic	Detrital	Authigenic	Detrital
O	46.47	48.33	46.52	49.63	49.16	45.57	48.08	46.2	49.47	45.76	46.1	44.9	45.93
N	0.07	2.75	0.15	5.17	4.14	0.59	2.72	0.15	3.22	0.51	0.17	0.51	0.13
K	9.18	6.51	12.25	1.50	3.49	12.46	6.90	11.49	5.26	12.64	11.73	12.66	12.81
Fe	0.16	0.05	0.00	0.00	0.00	0.02	0.00	0.03	0.02	0.01	0.03	0.03	0.03
Na	2.60	0.08	0.89	0.01	0.05	0.20	0.080	1.62	0.01	0.05	1.41	0.07	0.49
Si	30.52	31.32	30.26	32.60	31.95	30.74	31.76	30.85	31.48	30.44	30.48	30.31	30.05
Ca	0.15	0.01	0.01	0.01	0.02	0.00	0.00	0.05	0.00	0.00	0.07	0.03	0.00
Al	9.88	9.94	9.85	10.07	10.03	9.89	9.98	9.77	10.01	9.85	9.91	9.97	9.87
Ba	0.45	0.39	0.34	0.13	0.18	0.25	0.29	0.02	0.42	0.68	0.11	1.28	1.06
Total	99.49	99.39	100.26	99.12	99.01	99.70	99.80	100.16	99.89	99.94	100.01	99.76	100.38
Structural formula based on a total of 13 cations and anions (excluding Ti, Mg, and Mn)													
N	0.00	0.51	0.01	0.94	0.76	0.10	0.50	0.01	0.59	0.08	0.01	0.08	0.01
Na	0.31	0.01	0.11	0.00	0.01	0.02	0.01	0.19	0.00	0.01	0.170	0.01	0.06
K	0.65	0.44	0.87	0.10	0.23	0.89	0.47	0.81	0.35	0.90	0.83	0.91	0.91
Ba	0.01	0.01	0.01	0.00	0.00	0.01	0.01	0.00	0.01	0.01	0.00	0.03	0.02
Ca	0.01	0.00	0.00	0.00	0.00	0.00	0.00	0.00	0.00	0.00	0.01	0.00	0.00
Al	1.01	0.98	1.01	0.96	0.97	1.02	0.99	1.00	0.98	1.02	1.02	1.04	1.02
Fe	0.01	0.00	0.00	0.00	0.00	0.00	0.00	0.00	0.00	0.00	0.00	0.00	0.00
Si	3.00	2.98	2.97	2.99	2.98	3.04	3.02	3.03	2.95	3.02	3.00	3.03	2.98
O	8.01	8.07	8.03	8.00	8.05	7.92	8.01	7.96	8.13	7.96	7.96	7.89	8.00
Total	13.00	13.00	13.00	13.00	13.00	13.00	13.00	13.00	13.00	13.00	13.00	13.00	13.00
A site—N	0.98	0.46	0.98	0.10	0.24	0.92	0.49	1.01	0.36	0.92	1.01	0.95	0.99
A site	0.98	0.97	0.99	1.04	1.00	1.01	0.98	1.02	0.95	1.00	1.02	1.03	1.00
T site	4.01	3.96	3.98	3.96	3.95	4.06	4.00	4.03	3.92	4.03	4.02	4.08	4.00
% Budd	0	53	1	90	76	10	51	1	62	8	1	8	1
% Kfs	66	46	88	10	23	88	48	79	37	90	81	88	91
% Ab	32	1	11	0	1	2	1	19	0	1	17	1	6
% Cel	1	1	1	0	0	1	1	0	1	1	1		2
% An	1	0	0	0	0	0	0	0	0	0	0	0	0
Detection limits (ppm)													
N	794	894	730	964	986	792	920	746	930	784	736	748	736
Na	292	238	242	266	264	282	270	294	256	256	266	274	266
Ba	626	470	522	488	544	550	540	546	528	564	550	580	584

Sample wt%	KO2HS-22 Authigentic	KO2HS-26 Detrital	KO2HS-26 Authigenic	KO2HS-19 Authigenic	KO2HS-19 Authigenic	KO2HS-28 Detrital	KO2HS-2N Authigenic	KO2HS-29 Detrital	KO2HS-29 Authigenic	KO2HS-16 Detrital	KO2HS-I6 Authigenic	B-11 Detrital	B-11 Authigenic
O	46.67	45.80	46.85	49.06	49.33	46.13	47.54	45.77	46.81	46.13	47.81	45.49	48.32
N	1.63	0.09	1.49	4.50	4.57	0.17	2.14	0.06	1.38	0.06	3.02	0.17	1.42
K	9.47	13.11	9.87	2.58	2.19	12.41	8.30	12.79	10.05	12.91	5.97	12.52	9.67
Fe	0.08	0.01	0.01	0.00	0.03	0.00	0.05	0.09	0.01	0.11	0.08	0.00	0.03
Na	0.05	0.50	0.10	0.06	0.08	0.98	0.10	0.48	0.14	0.61	0.05	0.71	0.12
Si	31.70	30.60	31.88	32.42	32.26	30.42	30.99	29.81	31.22	30.15	31.41	29.57	31.42
Ca	0.00	0.00	0.00	0.01	0.00	0.02	0.00	0.00	0.00	0.02	0.00	0.00	0.00
Al	9.56	9.76	9.36	10.29	10.09	9.84	9.77	9.94	9.69	9.66	9.80	9.70	9.47
Ba	0.09	0.05	0.08	0.02	0.04	0.25	0.75	1.39	0.28	0.15	0.62	1.17	0.11
Total	99.25	99.92	99.64	98.94	98.58	100.22	99.64	100.33	99.58	99.79	98.75	99.32	100.56
Structural formula based on a total of 13 cations and anions (excluding Ti, Mg, and Mn)													
N	0.30	0.00	0.27	0.82	0.83	0.01	0.40	0.00	0.25	0.00	0.56	0.01	0.25
Na	0.01	0.06	0.01	0.01	0.01	0.12	0.01	0.06	0.02	0.07	0.01	0.09	0.01
K	0.66	0.93	0.69	0.17	0.15	0.88	0.57	0.91	0.70	0.92	0.41	0.90	0.66
Ba	0.00	0.00	0.00	0.00	0.00	0.01	0.02	0.03	0.01	0.00	0.01	0.02	0.00
Ca	0.00	0.00	0.00	0.00	0.00	0.00	0.00	0.00	0.00	0.00	0.00	0.00	0.00
Al	0.97	1.01	0.95	0.99	0.98	1.01	0.98	1.03	0.98	1.00	0.98	1.01	0.94
Fe	0.00	0.00	0.00	0.00	0.00	0.00	0.00	0.00	0.00	0.01	0.00	0.00	0.00
Si	3.08	3.03	3.10	3.01	2.99	3.00	2.98	2.97	3.04	2.98	3.00	2.96	3.01
O	7.97	7.97	7.98	8.00	8.04	7.98	8.04	8.00	8.00	8.02	8.03	8.00	8.12
Total	13.00	13.00	13.00	13.00	13.00	13.00	13.00	13.00	13.00	13.00	13.00	13.00	13.00
A site—N	0.67	1.00	0.70	0.18	0.16	1.00	0.60	1.00	0.72	1.00	0.43	1.01	0.68
A site	0.97	1.00	0.98	1.00	0.99	1.02	1.00	1.00	0.98	1.00	0.99	1.03	0.93
T site	4.06	4.04	4.04	4.00	3.98	4.01	3.97	4.00	4.02	3.99	3.98	3.97	3.95
% Budd	31	0	28	82	84	1	40	0	26	0	57	1	27
% Kfs	68	93	70	17	15	86	57	91	72	92	41	87	71
% Ab	1	6	1	1	1	11	1	6	2	7	1	8	1
% Cel	0	0	0	0	0	0	2	3	1	0	1	2	0
% An	0	0	0	0	0	0	0	0	0	0	0	0	0
Detection limits (ppm)													
N	822	774	822	964	996	730	836	768	792	744	900	726	770
Na	254	286	232	256	226	254	268	260	258	278	292	252	270
Ba	506	546	516	279	482	558	550	576	532	576	514	558	530

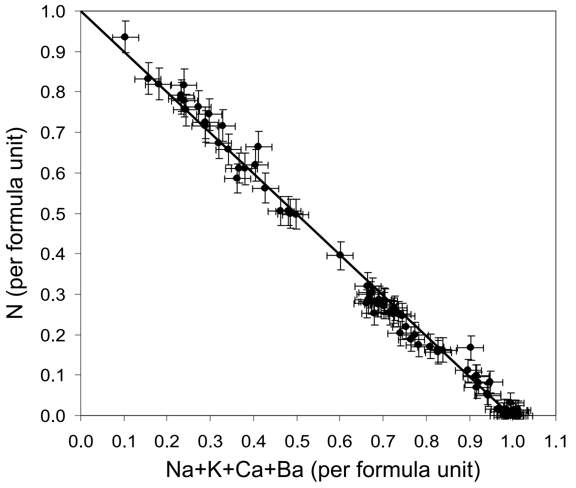

Fig. 8. Calculated structural formulas show that the A site in the authigenic feldspar range from being entirely filled by K to contain up to 95 mole % N per formula unit. There are no systematic variations between the buddingtonite component and rock type.

by previous workers (Turner, 1972; Sali Lorentzen, 2004), we suggest that the flood basalt cover was thicker than the proposed minimum of 1.4 km (Johnson et al., 1997), or that the geothermal gradient was higher than about 50 °C/km. The latter is not realistic as it would have produced low-grade metamorphic mineral assemblages as shallow as 3–4 km in the basin. Even chlorite formation in sandstone may occur at temperatures as low as 90–100 °C (e.g., Aagaard et al., 2000). However, a pulse of hot fluids could have precipitated the quartz without affecting the regional geothermal gradient. The formation of illite could have been caused by recrystallization of smectite, or precipitated directly from NH_4^+-rich solutions possibly associated with petroleum generation (cf, Schroeder and McLain, 1998).

5.3. Light element geochemistry of contact metamorphic shale

The new data on the N geochemistry of contact metamorphic Ecca Group black shale show that there is an isotopic shift of up to 10‰ caused by the heating. However, it appears that a threshold level of metamorphism corresponding to 3.4–4%Ro was reached before the shift occurred. Thus the shale was heated to beyond the gas window before significant isotopic shift occurred. When comparing Figs. 10A and B, this threshold corresponds to the heating level where the content of organic matter is dramatically reduced due to C gas formation. At the same time, the geochemical behaviors of C and N differ significantly. Whereas the bulk TOC content is mainly controlled by metamorphic grade, a significant fraction of the N remains in the shale, likely incorporated into metamorphic minerals as NH_4^+ ions. For example, sample KL1/78/04-87.15 has a very high reflectivity of

Table 3
Mineral content and nitrogen geochemistry of rocks and minerals from hydrothermal vent complexes

Sample	Mineralogy (XRD)[a]	Microprobe analysis			Isotope analysis			
		Buddingtonite			<63 µm	N (ppm)	>63 µm	N (ppm)
		No. of points	wt% N max	N pfu max[b]	$\delta^{15}N$		$\delta^{15}N$	
Vent sandstone facies								
K01HS-56	Budd, illite, (chl)	12	3.88	0.73	9.3	1585	9.1	642
K02HS-29	Budd, illite	9	2.76	0.52	9.5	1655	9.0	1115
Sediment breccia facies (clast)								
K02HS-15	Budd, illite chl	16	3.99	0.76	9.0	886	8.4	713
Sediment breccia facies								
K02HS-16	Illite, chl, budd	13	3.32	0.64	9.2	1452	8.5	903
B-11	n.a.	4	1.55	0.30	7.5	972	7.9	689
Pipes and dykes								
K02HS-19	Budd, illite	5	4.64	0.87	10.6	2003	10.2	1338
K02HS-22	Budd, illite	3	1.63	0.32	9.4	1379	8.7	930
K02HS-26	Budd, illite	5	1.49	0.29	8.9	1623	8.7	950
K02HS-28	Budd, illite	8	2.14	0.41	9.5	1758	9.0	1096
K03HS-22	Budd	3	3.31	0.64	7.7	952	7.5	534
Clarens and Elliot in Witkop III area								
K01HS-47	Budd	17	5.17	0.95	3.6	5959	4.8	1048
HS-35	Illite, laumontite				4.9	2522	4.6	2400
HS-I91	Illite, chl				4.4	734	3.7	684
HS-216	Illite, chl				1.6	1819	1.5	1787
HS-259	Illite				2.6	596	2.2	572

[a] Bulk and clay fraction XRD analyses. The buddingtonite is identified by EMP. *Abbreviations:* budd, buddingtonite; chl, chlorite (parantheses indicate low modal content).

[b] Maximum nitrogen content per formula unit (pfu).

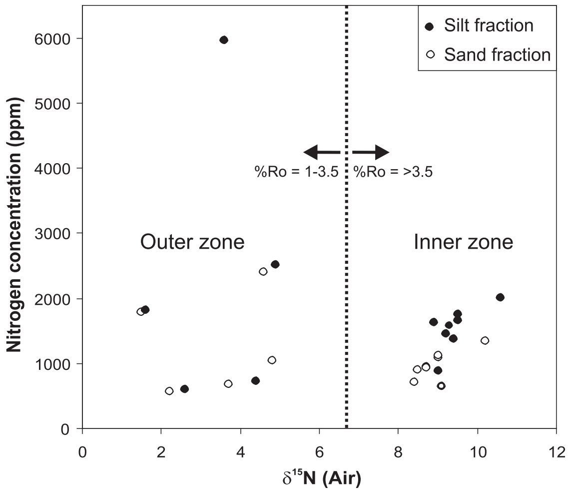

Fig. 9. The results from the silt and sand fraction N geochemical analyses show a vide range in both N concentrations and δ^{15}N. The results can be grouped according to geological setting at Witkop III. Group I results come from the outer zone of the hydrothermal vent complex, and Group II from the inner zone. Within the two groups, the illite (silt fraction) and the buddingtonite (sand fraction) show very similar δ^{15}N values, but illite is commonly up to 0.7‰ enriched compared to buddingtonite. The spread in δ^{15}N values is higher within Group II sediment breccias that in the sandstones. The vertical dotted line shows the corresponding δ^{15}N values of contact metamorphic shale with low (<3.5%Ro) and high (>3.5%Ro) vitrinite reflectance (data from Table 4).

7.7%Ro, and contains essentially no organic C, whereas the N concentration is 528 ppm (Table 4). The N/TOC data do however not provide a reliable measure of how much N was lost from the sediments in the aureole case study (Fig. 10B). From the isotopic data, a 10‰ increase in δ^{15}N relative to the protolith would require a high degree of N loss from the rocks, independent of the actual devolatilization mechanism (i.e., Rayleigh distillation or batch devolatilization; see demonstration in Fig. 11; (cf. Bebout et al., 1999). The magntitude of the isotopic shift would, however, depend on the fluid–rock N isotope fractionation factor, which is in turn dependent on temperature (Fig. 11). The trend of increasing δ^{15}N with metamorphic grade is consistent with that documented for metamorphic systems subjected to greenschist- and higher-grade conditions (e.g., Bebout and Fogel, 1992; Bebout et al., 1999; Jia, 2006). For contact aureoles around plutons, δ^{15}N values above ~8‰ are only found within a few meters of the contact (Haendel et al., 1986; Bebout et al., 1999). The N gases released from the contact aureole during devolatilization will be isotopically lighter than the background rocks during early metamorphism. However, as the heating continues, the N released into fluids will gradually be enriched in ^{15}N (see curve in Fig. 11 labeled, "Fluid N_2 for Rayleigh 600 °C Model" (cf. Haendel et al., 1986; Bebout and Fogel, 1992).

5.4. Nitrogen sources

The N isotope compositions of buddingtonite and illite could help discriminate between different N sources and reservoirs in the Karoo Basin. These potential sources include: (1) clay minerals from the Stormberg Group sediments, (2) sedimentary pore fluids equilibrated within the overlying flood basalts, or mantle-derived N released from dolerite sills during crystallization, (3) petroleum migrated

Table 4
Nitrogen and organic geochemistry of bulk-rock and kerogen extracts from contact aureoles

Borehole/sample (m)	N (ppm)	δ^{15}N (‰)	%Ro	St. dev.	TOC (wt%)	N/TOC
KL1/78/04—61.85 Bulk	472.8	5.0	1.27	0.10	0.44	0.107
KL1/78/04—67.85 Bulk	1421.0	14.2	4.42	0.42	4.35	0.033
KL1/78/04—87.15 Bulk	528.3	14.2	7.70	0.68	0.01	5.283
KL1/78/04—92.6 Bulk	627.4	4.7	3.60	0.20	1.01	0.062
KL1/78/04—94.7 Bulk	639.5	5.3	2.80	0.23	1.07	0.060
KL1/78/04—103.6 Bulk	782.8	4.5	1.68	0.14	2.18	0.036
KL1/78/04—126.75 Bulk	801.9	4.4	1.34	0.14	2.77	0.029
KL1/78/04—61.85 Kerogen	553.4	4.6	1.27	0.10		
KL1/78/04—67.85 Kerogen	1921.6	10.9	4.42	0.42		
KL1/78/04—94.7 Kerogen	556.8	4.9	2.80	0.23		
KL1/78/04—103.6 Kerogen	1062.2	4.2	1.68	0.14		
KL1/78/04—126.27 Kerogen	1110.1	3.8	1.34	0.14		
G39974/04—238.3 Bulk	1716.7	6.5	4.34	0.30	0.45	0.381
G39974/04—273.22 Bulk	4590.8	12.5	4.53	0.43	0.40	1.147
G39974/04—322.5 Bulk	2626.4	8.2	4.53	0.52	0.57	0.461
G39974/04—372 Bulk	5245.8	11.8	4.65	0.34	6.34	0.083
G39974/04—393.26 Bulk	2012.9	11.1	4.64	0.38	1.18	0.171
G39974/04—402.11 Bulk	2305.3	11.8	4.08	0.56	2.28	0.101
G39974/04—4l5.7 Bulk	946.2	12.7	7.90	0.49	0.01	9.462
G39974/04—534.4 Bulk	1344.23	14.2	7.58	0.66	0.03	4.481
G39974/04—322.5 Kerogen	1475.3	8.2	4.53	0.52		
G39974/04—363.4 Kerogen	2880.7	11.8	4.61	0.36		
G39974/04—381.39 Kerogen	4240.3	11.8	5.03	0.45		

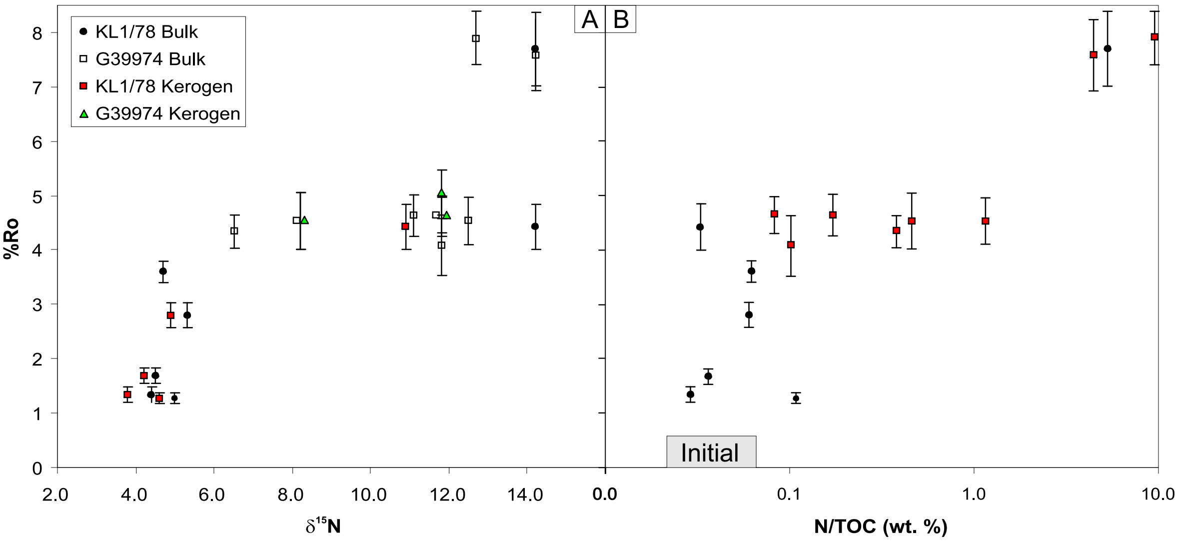

Fig. 10. Geochemistry of contact metamorphic rocks. (A) The δ^{15}N varies with the vitrinite reflectance (an indirect measure of the diagenetic/metamorphic grade). Samples subjected to high temperatures show a considerable fractionation of N isotope. (B) The N/TOC ratio varies with the maturity, and reflects the loss of C from the rocks during heating. The effect is pronounced above %Ro of 4.

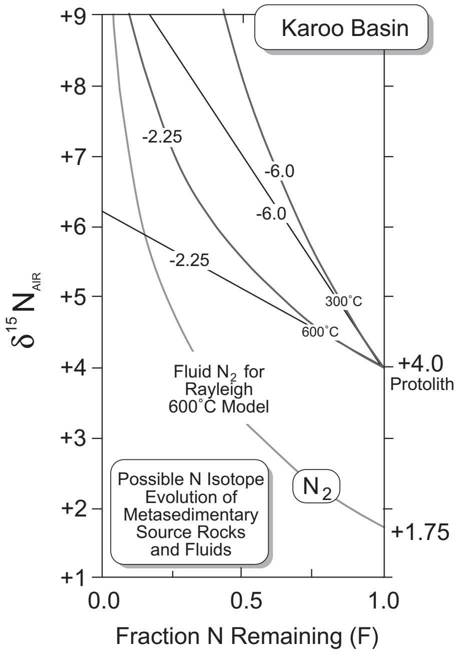

Fig. 11. Calculated rock and fluid δ^{15}N as functions of the extent of N loss from devolatilizing sediments, at temperatures of 300 and 600 °C, using the fractionation data from Hanschmann (1981). For each temperature (300 and 600 °C), curved lines are for Rayleigh distillation and straight lines are for batch loss (see discussion of the two models by Bebout and Fogel, 1992). See text for discussion.

from deeper levels in the basin, and (4) N derived from metamorphic devolatilization reactions or from organic-rich sedimentary rocks. We favor metamorphic devolatilization triggered by sill emplacement as the primary source of N found in inner-zone rocks. However, here we first briefly discuss the plausibility of sources 1–3.

In the case of a local clay mineral source (i.e., from the Stormberg Group sediments) for the N, we would anticipate that the N fixed in the diagenetic buddingtonite and illite would have the same δ^{15}N values as the organic matter (cf. Williams et al., 1995). The outer zone δ^{15}N values are similar to typical sedimentary values where the ultimate primary N source is organic matter but clay minerals now house a considerable fraction of the N as NH_4^+ (e.g., Williams et al., 1995). However, the N isotope composition of the inner and outer zone rocks differ strongly (Fig. 9), suggesting either (1) open system behavior in the HVC and derivation of N from different reservoirs or (2) considerably higher initial N concentrations and lower δ^{15}N values in inner-zone lithologies, both of which were then modified by metamorphic devolatilization. The latter mechanism is unlikely as the inner-zone sedimentary rocks have not undergone metamorphism at sufficiently high grades to result in major metamorphic fluid release. A source from local organic matter is not likely as the Clarens formation is dominated by aeolian sand and silt (e.g., Dingle et al., 1983; Veevers et al., 1994). The Elliot formation contains abundant shale horizons which are potential sources of N during diagenesis, but most Elliot Fm. shales are oxidized and contain little or no organic C. We conclude that the most likely reservoir and source for the outer zone N is organic, with a large fraction of the originally organic N now sited in clays. The inner zone N requires a different explanation, most plausibly involving introduction of nitrogen from an external source.

Nitrogen in basalts commonly shows a wide range in δ^{15}N (Faure and Mensing, 2005). However, the mantle reservoir is depleted in ^{15}N compared to air with a δ^{15}N value of $\sim -5‰$ (Marty and Dauphas, 2003), although values as low as $-9‰$ have been suggested (Faure and Mensing, 2005). Thus the N isotope compositions of inner and outer zone rocks are inconsistent with significant N sourcing from cooling/degassing lavas or dolerite sills.

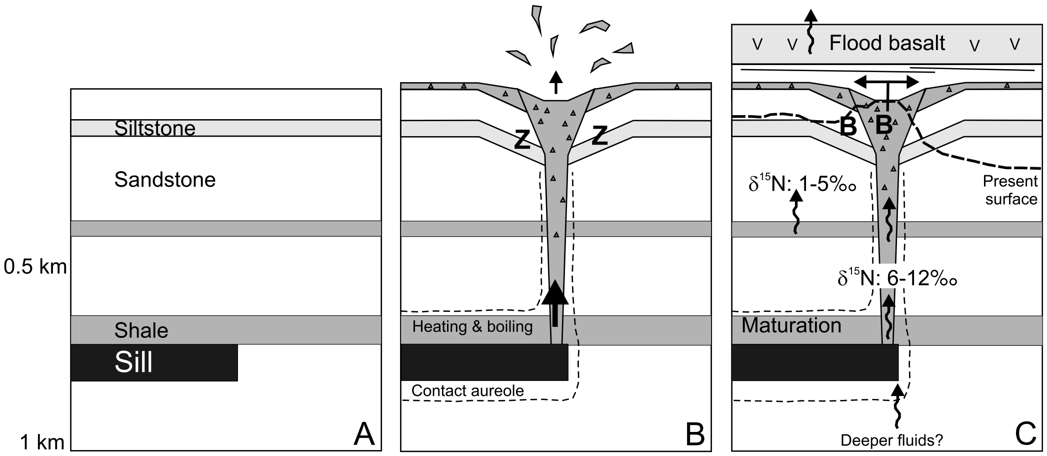

Fig. 12. Time series representation of the evolution of the Karoo hydrothermal vents in response to the emplacement of mafic sills resulting in rapid devolatilization of surrounding sedimentary rocks. See text for discussion.

Coal-bearing horizons are known to occur as <0.5-m-thick seams in Easter Cape (e.g., Dingle et al., 1983), and are thus a potential source for the inner zone N. The coal seams and the maturation of the organic matter in the Ecca Group shale likely generated petroleum-bearing fluids, which would also be N-bearing. However, because N released from organic matter during early diagenesis is strongly ^{15}N depleted (Zhu et al., 2000), both the coal seams and the Ecca Group shales can be ruled out as the source of N found in the inner-zone rocks. During further maturation, the generated petroleum will have the same N isotopic composition as the bitumen it was derived from, whereas secondary migration may cause ^{15}N enrichment due to interaction with sediments (Williams et al., 1995). Thus to explain the inner zone N isotope data with a petroleum source, a ^{15}N-enriched source rock or fluid–rock interactions during migration is required.

5.5. Preferred scenario for the nitrogen release and inner-zone nitrogen enrichment

We believe that the transport of the deeply-sourced metamorphic fluids upward through the vent complex and its surroundings during early burial diagenesis resulted in the precipitation of early diagenetic, ^{15}N-enriched buddingtonite ($\delta^{15}N = +7.5‰$ to $+10.2‰$) and somewhat later-formed illite. As one means of evaluating the deeper metamorphic dehydration of the Ecca Group and Molteno coal as a N source, we examined the behavior of N in contact metamorphic aureoles developed in similar rocks. As discussed above, and demonstrated in Fig. 11, the loss of N as N_2 during metamorphic devolatilization can result in shifts of sedimentary rock δ^{15}N toward higher values. Moreover, fluids released by devolatilization will become increasingly rich in ^{15}N as devolatilization progresses (Fig. 11; (see also Haendel et al., 1986; Bebout and Fogel, 1992; Krooss et al., 1995; Bebout et al., 1999). In general, it appears that the loss of N from the appropriate sedimentary lithologies, over the approximate temperature range of 300–600 °C, with "*F*" (fraction of the original sediment N remaining) as low as 0.20 (and particularly if NH_3 was the dominant N fluid species), could certainly have produced upward δ^{15}N shifts of up to 10‰ as observed in the contact aureoles. This would shift the sediments to values near +14‰ (see δ^{15}N data in Fig. 10A).

Fig. 12 illustrates our view of the evolution of the Karoo hydrothermal vent complexes in response to the intrusion of mafic sills at depth. Contact metamorphism of organic-rich sedimentary rocks adjacent to the sills resulted in dramatic volatile loss and related N depletion and N isotope modification of the heated sediments. The released fluids would then have been driven by buoyancy towards the surface and have interacted with HVC lithologies during transport. We suggest that these vent complexes would have remained highly permeable avenues for the upward transport of fluid long after the major pulse of fluid release. If fluids released by deep-seated rocks at 600 °C contained N_2 as the dominant N fluid species, this N_2 would likely have had δ^{15}N values between about +1.75‰ and +6 ‰. This range of δ^{15}N values is compatible with sedimentary rocks that have lost between 0% and 80% of their N by devolatilization (Fig. 11). The N isotope composition of NH_4-rich silicate phases stabilized along the transport path of the ascending fluids would be controlled by the δ^{15}N values of these fluids and the temperature dependent NH_4–N_2 nitrogen isotope fractionation factor. For example, NH_4-bearing silicates formed at 300 °C in isotopic equilibrium with infiltrating N_2 fluids would have δ^{15}N values ~6‰ higher than these fluids (~+7.75‰ to +12‰). Equilibration of the same N_2-bearing metamorphic fluids with NH_4^+-rich silicates at temperatures lower than 300 °C would likely have produced even higher δ^{15}N for the silicate phases. The magnitudes of the fluid–mineral fractionations are largely unknown for the temperature range of 100–300 °C. The coexistence of NH_4-rich silicates and fluids containing molecular N (N_2) has previously been documented for low-grade metamorphic settings (e.g., Darimont et al., 1988; Bebout, 1997), but the details regarding the nature of the isotopic exchange between silicate NH_4 and fluid N_2, during such processes as devolatilization and metasomatic alteration, remain uncertain (see discussion of possible mechanisms by Boyd (1997)). Bebout and Sadofsky (2004) reported N isotope compositions of fluid inclusion N_2 and vein biotite NH_4 that appear to reflect isotopic equilibrium between the vein fluids and silicates, with the difference between the biotite and the N_2 $\delta^{15}N$ values approximating values calculated for the temperature inferred for vein formation (using the fractionation factors calculated by Hanschmann (1981)). Kreulen et al. (1986) similarly suggested at least crude N isotope equilibrium between NH_4-rich silicates and fluid inclusion N_2. Bebout (1997) inferred the metasomatic replacement of plagioclase by NH_4-rich phengite (Si-rich potassic white-mica), with the N delivered to the mica by N_2-bearing metamorphic fluids (at temperatures near 350 °C).

It is possible that, under the low-temperature (perhaps ~70–80 °C) and more reducing conditions stabilizing the inner-zone buddingtonite, N in the fluid phase would have been speciated largely as NH_3 or NH_4, affecting the nature of the fluid–mineral N-isotope fractionation during the crystallization of buddingtonite. Metamorphic N_2 derived from greater depths could have, during its ascent, mixed with more locally-derived NH_4 and itself been re-speciated. Any N isotope fractionation accompanying this mixing and re-speciation is difficult to evaluate as the details regarding the isotope exchange model are lacking. However, it is conceivable that the resulting NH_4 would have at least crudely borne the N-isotope signature of the N_2-bearing fluids infiltrating from depth (+1.75‰ to +6‰ for the fluid loss model described above). Fluid–rock interaction along the upward flow path of these fluids, or mixing of the fluids derived by metamorphic devolatilization with fluids produced by other processes (e.g., release of N from rocks in and near the HVC in response to heating by the warm ascending fluids), could have resulted in fluids with $\delta^{15}N$ values appropriate for producing the $\delta^{15}N$ range found in the inner-zone diagenetic NH_4^+-rich phases (see Fig. 12C). We believe that illite formed during later burial or deeper in the basin at conditions corresponding to the oil window (60–120 °C), but incorporated N from the same largely deep-basinal N source as the earlier-formed buddingtonite. This explains the fact that the Group II illite and buddingtonite have similar $\delta^{15}N$ values even though the timing of precipitation is likely different.

5.6. Implications for fluid migration

The presence of buddingtonite demonstrates that diagenetic fluids were NH_4^+-bearing and reducing, with high NH_4^+/H^+ and K^+/H^+ activity ratios (Mader et al., 1996). As discussed above, the most likely mechanism to explain the formation of buddingtonite within the vent complex is seepage of fluids with a devolatilization origin through the HVC. High NH_4^+ concentrations in petroleum-bearing fluids are known from both active hydrothermal systems in sedimentary basins (Von Damm et al., 1985) and from petroleum provinces (e.g., Williams et al., 1995). Our data show that the hydrothermal vent complexes formed new fluid flow pathways in the Karoo Basin, with the ability to focus fluids from deeper in the basin. This is in line with results from the Norwegian Sea, where a prolonged seep history is recorded by carbonates above a hydrothermal vent complex (Svensen et al., 2003). In this respect, the HVC share some similarities with mud volcanoes in the dormant period, where gas and liquid migrates upward from considerable depths (e.g., Planke et al., 2003). The mineralogical record of N-bearing phases is limited to the temperature–depth interval corresponding to buddingtonite and illite stability, but we cannot exclude the possibility that the vent complexes acted as longterm fluid flow pathway for N-bearing fluids. This conclusion is supported by data from a phreatomagmatic pipe structure in the Ladybrand area, where the pipe structure is one of the few known active petroleum seeps in the Karoo Basin (Woodford et al., 2001).

5.7. Implications for the geochemical cycle of nitrogen

Considering that the considerable mass of N bound in rocks (e.g., Holloway and Dahlgren, 2002), devolatilization of N-bearing shale is potentially an important part of the geochemical cycle of N at least during the formation of large igneous provinces and associated volcanic basins. Constraints on the N mobilization from the Karoo Basin can be derived from the data presented by Svensen et al. (2007), stating that between 294 and 505 Gt C vented from the Western Karoo Basin during contact metamorphism of the Ecca Group. The production potential for the whole Karoo Basin is between 1870 and 7490 Gt C, and the carbon gas venting may have triggered or contributed to early Jurassic global warming. By assuming a N/TOC ratio of 0.03 for the bulk of the Ecca Group (Fig. 10), and that at least 50% of the initial N was removed during devolatilization, we can estimate the total mass of mobilized N. For the Western Karoo case, the potentially mobilized N is between 1.5 and 2.5 Gt N, whereas the production potential for the whole Karoo Basin is between 9.4 and 37.5 Gt N. Compared to the N flux from volcanoes along the Central American convergent margin of 8.2×10^{-6} Gt/year (Hilton et al., 2002), the total release from the Karoo Basin correspond to 0.2–4.7 m.y. of this volcanic degassing.

6. CONCLUSIONS

- The authigenic petrography of sandstone and breccia from an early Jurassic hydrothermal vent complex documents that NH_4^+ feldspar formed during early diagenesis and mechanical compaction. The buddingtonite occurs in fractured K-feldspar grains and as overgrowths, and is found within sandstone and sediment breccia matrix and clasts.
- The authigenic feldspar contains up to 90 mole % buddingtonite. Isotope analyses of the sand fraction of the samples represent an approximation to buddingtonite $\delta^{15}N$ values, and the samples fall in two distinct groups according to geological setting. Group I samples are from outside the vent complex ($\delta^{15}N$ between +1.5‰ and +4.6‰), and Group II samples from inside the complex ($\delta^{15}N$ between +7.1‰ and +10.2‰).

- The silt and clay fraction of the samples always have the highest N concentrations, and the main clay mineral is illite. The δ^{15}N of illite is 0.7‰ higher than that of buddingtonite.
- Data from contact metamorphosed Ecca Group shale demonstrate an up to 10‰ fractionation of N isotopes during heating, providing an analog for the isotopic shifts of rocks and fluids produced by devolatilization of inferred fluid sources below the HVC. We propose that N_2 with relatively high δ^{15}N capable of producing the δ^{15}N range of the buddingtonite was formed during metamorphic devolatilization of organic-rich sedimentary rocks.
- Details regarding fluid–mineral exchange and fluid mixing along the upward flow paths are lacking, and it is likely that N_2 ascending from depths would have re-speciated as NH_3 or NH_4 in the fluid phase at the low-temperature and reducing conditions at which buddingtonite formed. However, it appears likely that these ascending N-bearing fluids retained the N isotope signature of metamorphic devolatilization and imparted this signature on buddingtonite and illite crystallized in equilibrium with these fluids at lower temperatures.
- Nitrogen geochemistry in general, and the geochemistry of buddingtonite in particular, are useful tracers of paleo-fluid flow in sedimentary basins, and has implications for the geochemical cycling of N. Such studies are especially important if basin formation is associated with periods of intense volcanic activity. The hydrothermal vent complex drained fluid from deep basin levels, a process which is still occurring locally in the Karoo Basin.

ACKNOWLEDGMENTS

This study was supported by two PetroMaks grants (to A. Malthe-Sørenssen and H. Svensen; 169457/S30) and a Centre of Excellence grant (to PGP), all from the Norwegian Research Council. The N isotope analyses were funded by a grant to G.E.B. from the USA National Science Foundation (EAR-0409008). We thank Goonie Marsh for discussions and support during field work in South Africa, the Department of Water Affairs and the Council for Geoscience (South Africa) for borehole drilling at Witkop III and access to cores (handled by David Motloi). We also thank Doug Cole for discussions about the geology of the Karoo Basin, Stephane Polteau, and Dirk Liss for assistance during field work, and Adriano Mazzini, Robert Kerrich, Tom Chacko, and an anonymous referee for improving the manuscript.

REFERENCES

Aagaard P., Jahren J. S., Harstad A. O., Nilsen O. and Ramm M. (2000) Formation of grain-coating chlorite in sandstones. Laboratory synthesized vs. natural occurrences. *Clay Miner.* **35**, 261–269.

Armstrong J. T. (1988) *Accurate Quantitative Analysis of Oxygen and Nitrogen with a W/Si Multilayer Crystal*. San Francisco Inc., San Francisco.

Armstrong J. T. (1995) Citzaf—a package of correction programs for the quantitative electron, microbeam X-ray-analysis of thick polished materials, thin-films, and particles. *Microbeam Anal.* **4**, 177–200.

Arnaud N. O. and Kelley S. P. (1997) Argon behaviour in gem-quality orthoclase from Madagascar: experiments and some consequences for Ar-40/Ar-39 geochronology. *Geochim. Cosmochim. Acta* **61**, 3227–3255.

Bastin G. F. and Heijligers H. J. M. (1988) *Quantitative Electron Probe Microanalysis of Nitrogen*. University of Technology Eindhoven, Laboratory of Solid State Chemistry and Material Science, Eindhoven, The Netherlands.

Bebout G. E. (1997) Nitrogen isotope tracers of high-temperature fluid–rock interactions: case study of the Catalina Schist, California. *Earth Planet. Sci. Lett.* **151**, 77–91.

Bebout G. E. and Fogel M. L. (1992) Nitrogen-isotope compositions of metasedimentary rocks in the Catalina Schist, California—implications for metamorphic devolatilization history. *Geochim. Cosmochim. Acta* **56**, 2839–2849.

Bebout G. E. and Sadofsky S. J. (2004) Nitrogen isotope analyses of ammonium-rich silicate minerals by sealed-tube extractions and dual inlet, viscous-flow mass spectrometry. In *Handbook of Stable Isotope Techniques* (ed. P. de Groot). Elsevier, Amsterdam.

Bebout G. E., Cooper D. C., Bradley A. D. and Sadofsky S. J. (1999) Nitrogen-isotope record of fluid–rock interactions in the Skiddaw Aureole and granite, English Lake District. *Am. Miner.* **84**, 1495–1505.

Berndt C. (2005) Focused fluid flow in passive continental margins. *Philos. Trans. Roy. Soc. A-Math. Phys. Eng. Sci.* **363**, 2855–2871.

Boyd S. R. (1997) Determination of the ammonium content of potassic rocks and minerals by capacitance manometry: a prelude to the calibration of FTIR microscopes. *Chem. Geol.* **137**, 57–66.

Brown K. M. (1990) The nature and hydrogeologic significance of mud diapirs and diatremes for accretionary systems. *J. Geophys. Res.-Solid Earth Planets* **95**, 8969–8982.

Catuneanu O., Hancox P. J. and Rubidge B. S. (1998) Reciprocal flexural behaviour and contrasting stratigraphies: a new basin development model for the Karoo retroarc foreland system, South Africa. *Basin Res.* **10**, 417–439.

Chevallier L. and Woodford A. (1999) Morpho-tectonics and mechanism of emplacement of the dolerite rings and sills of the western Karoo, South Africa. *S. Afr. J. Geol.* **102**, 43–54.

Darimont A., Burke E. and Touret J. (1988) Nitrogen-rich metamorphic fluids in Devonian metasediments from Bastogne, Belgium. *Bull. Mineral.* **111**, 321–330.

Dingle R. V., Siesser W. G. and Newton A. R. (1983) *Mesozoic and Tertiary Geology of Southern Africa*. Balkema, Rotterdam.

Duncan R. A., Hooper P. R., Rehacek J., Marsh J. S. and Duncan A. R. (1997) The timing and duration of the Karoo igneous event, southern Gondwana. *J. Geophys. Res.* **102**, 18127–18138.

Elkins L. J., Fischer T. P., Hilton D. R., Sharp Z. D., McKnight S. and Walker J. (2006) Tracing nitrogen in volcanic and geothermal volatiles from the Nicaraguan volcanic front. *Geochim. Cosmochim. Acta* **70**, 5215–5235.

Faure K. and Cole D. (1999) Geochemical evidence for lacustrine microbial blooms in the vast Permian Main Karoo, Parana, Falkland Islands and Huab basins of southwestern Gondwana. *Palaeogeogr. Palaeoclimatol. Palaeoecol.* **152**, 189–213.

Faure G. and Mensing T. M. (2005) *Isotopes: Principles and Applications*, third ed. John Wiley and Sons, Inc., Hoboken, NJ.

Froelich P. N., Klinkhammer G. P., Bender M. L., Luedtke N. A., Heath G. R. and Cullen D., et al. (1979) Early oxidation of organic-matter in pelagic sediments of the eastern equatorial Atlantic—suboxic diagenesis. *Geochim. Cosmochim. Acta* **43**, 1075–1090.

Giles M. R., Indrelid S. L., Beynon G. V. and Amtor J. (2000) *The Origin of Large-scale Quartz Cementation: Evidence from Large Datasets and Coupled Heat–Fluid Mass Transport Modelling*. Blackwell Science, Oxford.

Haendel D., Muhle K., Nitzsche H. M., Stiehl G. and Wand U. (1986) Isotopic variations of the fixed nitrogen in metamorphic rocks. *Geochim. Cosmochim. Acta* **50**, 749–758.

Hanschmann G. (1981) Berechnung von Isotopieeffekten auf quantenchemischer Grundlage am Beispiel stick-stoffhaltiger Moleküle. *ZfI-Mitteilungen* **41**, 19–39.

Hilton D. R., Fischer T. P. and Marty B. (2002) Noble gases and volatile recycling at subduction zones. In *Noble Gases in Geochemistry and Cosmochemistry, Reviews in Mineralogy and Geochemistry* (ed. D. Porcelli, et al.). Rev. Mineral. Geochem., Mineral. Soc. America, Washington, DC.

Holloway J. M. and Dahlgren R. A. (2002) Nitrogen in rock: occurrences and biogeochemical implications. *Global Biogeochem. Cycles*, 16.

Hovland M., Talbot M. R., Qvale H., Olaussen S. and Aasberg L. (1987) Methane-related carbonate cements in pockmarks of the North Sea. *J. Sediment. Petrol.* **57**, 881–892.

Jakubov A. A., Ali-Zade A. A. and Zeinalov M. M. (1971) *Mud Volcanoes of the Azerbaijan SSR Atlas* (in Russian). Azerbaijan Academy of Sciences, Baku.

Jamtveit B., Svensen H., Podladchikov Y. and Planke S. (2004) Hydrothermal vent complexes associated with sill intrusions in sedimentary basins. *Geol. Soc. London, Spec. Publ.* **234**, 233–241.

Jia Y. (2006) Nitrogen isotope fractionations during progressive metamorphism: a case study from the Paleozoic Cooma metasedimentary complex, southeastern Australia. *Geochim. Cosmochim. Acta* **70**, 5201–5214.

Jia Y. and Kerrich R. (2004) Nitrogen 15-enriched Precambrian kerogen and hydrothermal systems. *Geochem. Geophys. Geosyst.* **5**, Q07005.

Jia Y., Kerrich R., Gupta A. K. and Fyfe W. S. (2003) ^{15}N-enriched Gondwana lamproites, eastern India: crustal N in the mantle source. *Earth Planet. Sci. Lett.* **215**, 43–56.

Johnson, M. R., Van Vuuren C. J., Visser J. N. J., Cole D. I., Wickens H. de V., Cristie A. D. M. and Roberts D. L. (1997) The foreland Karoo basin, South Africa. In *African basins*. Elsevier, Amsterdam.

Jourdan F., Feraud G., Bertrand H., Kampunzu A. B., Tshoso G. and Watkeys M. K., et al. (2005) Karoo large igneous province: brevity, origin, and relation to mass extinction questioned by new Ar-40/Ar-39 age data. *Geology* **33**, 745–748.

Kreulen R., Breemen A. V. and Duit W. (1986) Nitrogen and carbon isotopes in metamorphic fluids from the Dome de I'Agout, France. In *Geochronology, Cosmochronolgy and Isotope Geology, Fifth International Conference*, 191 pp.

Kronz A. and Pöter B. (1999) Wavelength-dispersive electron-microprobe-analysis of nitrogen on Buddingtonite–feldspar solid solution crystals. *Eur. J. Mineral.* **11**, 138.

Krooss B. M., Littke R., Muller B., Frielingsdorf J., Schwochau K. and Idiz E. F. (1995) Generation of nitrogen and methane from sedimentary organic matter: implications on the dynamics of natural gas accumulations. *Chem. Geol.* **126**, 291–318.

Leith M. J. and Trümpelmann F. (1967) *Well Completion Report for Southern Oil Exploration Corporation (PTY) Limited of WE 1/66*. Unpublished Report, Council for Geoscience, South Africa.

Loughnan F. C., Roberts F. I. and Lindner A. W. (1983) Buddingtonite (NH_4-Feldspar) in the Condor Oilshale Deposit, Queensland, Australia. *Mineral. Mag.* **47**, 327–334.

Mader U. K., Ramseyer K., Daniels E. J. and Althaus E. (1996) Gibbs free energy of buddingtonite ($NH_4AlSi_3O_8$) extrapolated from experiments and comparison to natural occurrences and polyhedral estimation. *Eur. J. Mineral.* **8**, 755–766.

Marty B. and Dauphas N. (2003) The nitrogen record of crust–mantle interaction and mantle convection from Archean to present. *Earth Planet. Sci. Lett.* **206**, 397–410.

Mazzini A., Aloisi G., Akhmanov G. G., Parnell J., Cronin B. T. and Murphy P. (2005) Integrated petrographic and geochemical record of hydrocarbon seepage on the Voring Plateau. *J. Geol. Soc.* **162**, 815–827.

Orberger B., Gallien J. P., Pinti D. L., Fialin M., Daudin L. and Grocke D. R., et al. (2005) Nitrogen and carbon partitioning in diagenetic and hydrothermal minerals from Paleozoic Black Shales (Selwyn Basin, Yukon Territories, Canada). *Chem. Geol.* **218**, 249–264.

Paull C. K., Chanton J. P., Neumann A. C., Coston J. A. and Martens C. S. (1992) Indicators of methane-derived carbonates and chemosynthetic organic carbon deposits: examples from the Florida escarpment. *Palaios* **7**, 361–375.

Planke S., Svensen H., Hovland M., Banks D. A. and Jamtveit B. (2003) Mud and fluid migration in active mud volcanoes in Azerbaijan. *Geo-Mar. Lett.* **23**, 258–268.

Planke S., Rassmussen T., Rey S. S. and Myklebust R. (2005) Seismic characteristics and distribution of volcanic intrusions and hydrothermal vent complexes in the Vøring and Møre basins. In *Petroleum Geology: North-West Europe and Global Perspectives—Proceedings of the Sixth Petroleum Geology Conference* (eds. B. Vining and T. Dore). Geological Society Publishing House, London.

Polteau S., Mazzini A., Galland O., Planke S. and Malthe-Sorenssen A. (2008) Saucer-shaped intrusions: occurrences, emplacement and implications. *Earth Planet. Sci. Lett.* **266**, 195–204.

Pöter B., Heinrich W., Gottschalk M. and Kronz A. (1999) Experimental determination of K^+–NH^{4+} distribution between feldspars and chloride solutions. *Eur. J. Mineral.* **11**, 179.

Ramseyer K., Diamond L. W. and Boles J. R. (1993) Authigenic K–NH_4–Feldspar in Sandstones—a fingerprint of the diagenesis of organic-matter. *J. Sediment. Petrol.* **63**, 1092–1099.

Raudsepp M. (1995) Recent advances in the electron-probe microanalysis of minerals for the light-elements. *Can. Mineral.* **33**, 203–218.

Rowsell D. M. and De Swardt A. M. J. (1976) Diagenesis in Cape and Karoo sediments, South Africa and its bearing on their hydrocarbon potential. *Trans. Geol. Soc. South Africa* **79**, 81–145.

Rybka R. and Wolf R. C. (1995) Application of layered synthetic microstructure crystals to WDX microanalysis of ultra-light elements. In *X-ray Spectrometry in Electron Beam Instruments* (eds. D. Wiliams, J. Goldstein and D. Newbury). Plenum, New York.

Sadofsky S. J. and Bebout G. E. (2000) Ammonium partitioning and nitrogen-isotope fractionation among coexisting micas during high-temperature fluid–rock interactions: examples from the New England Appalachians. *Geochim. Cosmochim. Acta* **64**, 2835–2849.

Sali Lorentzen S. A. (2004) *Petrographic and Petrophysical Properties of a Hydrothermal Vent Complex from the Karoo Basin, South Africa*. University of Oslo, Norway.

Schroeder P. A. and McLain A. A. (1998) Illite–smectites and the influence of burial diagenesis on the geochemical cycling of nitrogen. *Clay Miner.* **33**, 539–546.

Smith R. M. H. (1990) A review of stratigraphy and sedimentary environments of the Karoo Basin of South-Africa. *J. Afr. Earth Sci.* **10**, 117–137.

Svensen H., Planke S., Jamtveit B. and Pedersen T. (2003) Seep carbonate formation controlled by hydrothermal vent complexes: a case study from the Voring Basin, the Norwegian Sea. *Geo-Mar. Lett.* **23**, 351–358.

Svensen H., Planke S., Malthe-Sorenssen A., Jamtveit B., Myklebust R. and Rasmussen Eidem T., et al. (2004) Release of methane from a volcanic basin as a mechanism for initial Eocene global warming. *Nature* **429**, 542–545.

Svensen H., Jamtveit B., Planke S. and Chevallier L. (2006) Structure and evolution of hydrothermal vent complexes in the Karoo Basin, South Africa. *J. Geol. Soc.* **163**, 671–682.

Svensen H., Planke S., Chevallier L., Malthe-Sorenssen A., Corfu F. and Jamtveit B. (2007) Hydrothermal venting of greenhouse gases triggering Early Jurassic global warming. *Earth Planet. Sci. Lett.* **256**, 554–566.

Turner B. R. (1972) Silica diagenesis in the Molteno sandstone. *Trans. Geol. Soc. South Africa* **75**, 55–66.

Veevers J. J., Cole D. I. and Cowan E. J. (1994) *Southern Africa: Karoo Basin and Cape Fold Belt*. Geological Society of America, USA.

Von Damm K. L., Edmond J. M., Measures C. I. and Grant B. (1985) Chemistry of submarine hydrothermal solutions at Guaymas Basin, Gulf of California. *Geochim. Cosmochim. Acta* **49**, 2221–2237.

Walderhaug O. (1994) Temperatures of quartz cementation in Jurassic sandstones from the Norwegian Continental-Shelf—evidence from fluid inclusions. *J. Sediment. Res. A-Sediment. Petrol. Process.* **64**, 311–323.

Williams L. B., Ferrell R. E., Chinn E. W. and Sassen R. (1989) Fixed-ammonium in clays associated with crude oils. *Appl. Geochem.* **4**, 605–616.

Williams L. B., Wilcoxon B. R., Ferrell R. E. and Sassen R. (1992) Diagenesis of ammonium during hydrocarbon maturation and migration, Wilcox-Group, Louisiana, USA. *Appl. Geochem.* **7**, 123–134.

Williams L. B., Ferrell R. E., Hutcheon I., Bakel A. J., Walsh M. M. and Krouse H. R. (1995) Nitrogen isotope geochemistry of organic-matter and minerals during diagenesis and hydrocarbon migration. *Geochim. Cosmochim. Acta* **59**, 765–779.

Woodford A. C., Botha J. F., Chevallier L., Hartnady C., Johnson M. and Meyer R., et al. (2001) *Hydrogeology of the Main Karoo Basin: Current Knowledge and Research Needs*. Water Research Commission Report, South Africa, Pretoria.

Worden R. H. and Burley S. D. (2003) Sandstone diagenesis: the evolution of sand to stone. In *Sandstone Diagenesis* (eds. S. D. Burley and R. H. Worden). International Association of Sedimentologists, Reprint Volume 4.

Zhu Y. N., Shi B. Q. and Fang C. B. (2000) The isotopic compositions of molecular nitrogen: implications on their origins in natural gas accumulations. *Chem. Geol.* **164**, 321–330.

Associate editor: Thomas Chacko